

GEOPHYSICS®

Constrained ERT bayesian inversion using inverse Matérn covariance matrix

Journal:	<i>Geophysics</i>
Manuscript ID	GEO-2015-0673.R2
Manuscript Type:	Technical Paper
Date Submitted by the Author:	23-Jan-2017
Complete List of Authors:	Bouchedda, Abderrezak; INRS, Giroux, Bernard; INRS-ETE, ; Gloaguen, Erwan; INRS, ETE
Keywords:	electrical/resistivity, inversion, 2D, tomography
Area of Expertise:	Electrical and Electromagnetic Methods, Engineering and Environmental Geophysics

SCHOLARONE™
Manuscripts

Constrained ERT Bayesian inversion using inverse Matérn covariance matrix

Bouchedda Abderrezak, Institut national de la recherche scientifique, Centre Eau Terre Environnement, Quebec City, Canada. Abderrezak.Bouchedda@ete.inrs.ca.

Giroux Bernard, Institut national de la recherche scientifique, Centre Eau Terre Environnement, Quebec City, Canada. Bernard.Giroux@ete.inrs.ca.

Erwan Gloaguen, Institut national de la recherche scientifique, Centre Eau Terre Environnement, Quebec City, Canada. Erwan.Gloaguen@ete.inrs.ca.

Corresponding author

Bouchedda Abderrezak

Institut national de la recherche scientifique, Centre Eau Terre Environnement.
490, rue de la Couronne, G1K 9A9, Québec, Canada

Phone: +1-418-654-2609

E-mail: Abderrezak.Bouchedda@ete.inrs.ca

Submission date: 02 December 2015.

This paper was presented at **SEG 2015**, New Orleans.

1
2
3
4
5
6
7
8
9
10
11
12
13
14
15
16
17
18
19
20
21
22
23
24
25
26
27
28
29
30
31
32
33
34
35
36
37
38
39
40
41
42
43
44
45
46
47
48
49
50
51
52
53
54
55
56
57
58
59
60

ABSTRACT

Bayesian inversion using maximum a posteriori (MAP) estimator is a quantitative approach that has been successfully applied to the electrical resistivity tomography inverse problem. In most approaches, model covariance parameters are generally chosen stationary and isotropic, which assumes statistical homogeneity of studied field. However, the statistical properties of resistivity within the Earth are, in reality, location depend due to spatially varying processes that control the bulk resistivity of rocks, such as water content, porosity, clay content, etc. In order to take into account the spatial variability of the resistivity field, we propose to use the non-stationary Matérn covariance family that is defined through linear stochastic partial differential equations. Two types of prior information are considered, structure orientation and spatially increasing range with increasing depth. The latter is applied successfully on the first synthetic model which aims at retrieving the depth of bedrock and the shape of conductive lens. In the second synthetic example, a conductive dyke model embedded into four layers is used to study the performance of structure orientation. Finally, the proposed approach is used to invert real data measured over an extensively characterized sandy-to-silty aquifer. Structure orientation of this aquifer was firstly determined by applying structure tensor calculated using gradients of gpr image. The introduction of this information gives a resistivity model that is more compatible with the aquifer structure.

Keywords: electrical resistivity tomography, Bayesian inversion, Non-stationary Matérn precision matrix.

INTRODUCTION

Electrical Resistivity tomography (ERT) or electrical imaging is among the most commonly used high-resolution geophysical techniques in many geoscientific domains, such as hydrogeophysics (e.g. Binley and Kemna, 2005), engineering geophysics (e.g. Ramirez et al., 1996) or mining exploration (e.g. Oldenburg et al., 1997). An overview of recent ERT developments can be found in (Loke et al., 2013). ERT consists in the resolution of an inverse problem to estimate the spatial distribution of electrical resistivity within the ground, from measurements of electrical potential variations caused by the injection of an electric current into the ground.

The ERT inverse problem is ill-posed, nonlinear and underdetermined. Numerous inversion approaches have been published in the last three decades to tackle this problem (Loke et al., 2013). They can be separated in two groups: deterministic and stochastic approaches. Deterministic approaches are based commonly on the linearization of the forward problem operator using its first order Taylor expansion. The insufficiency of the ERT data to resolve the subsurface is commonly supplied (regularized) by the assumptions of model smoothness (e.g. Labrecque et al., 1996; Fridel, 2003) or blockiness (e.g. Loke et al., 2003). Thikonov regularization that produces smooth models is probably the most used for ERT and, more generally, in geophysical inversion. In stochastic approaches, all variables (data, model parameters and all related hyper-parameters) are modelled as random variables, which are encoded in terms of probability distributions. Generally, the solution of the inverse problem is obtained by maximizing the posterior probability distribution. Maximum likelihood (ML) and maximum a posteriori (MAP) estimators are the most popular methods (e.g. Ulrych et al., 2001;

1
2
3
4
5
6
7
8
9
10
11
12
13
14
15
16
17
18
19
20
21
22
23
24
25
26
27
28
29
30
31
32
33
34
35
36
37
38
39
40
41
42
43
44
45
46
47
48
49
50
51
52
53
54
55
56
57
58
59
60

1
2
3
4
5
6
7
8
9
10
11
12
13
14
15
16
17
18
19
20
21
22
23
24
25
26
27
28
29
30
31
32
33
34
35
36
37
38
39
40
41
42
43
44
45
46
47
48
49
50
51
52
53
54
55
56
57
58
59
60

Tarantola, 2005). Note that the MAP estimator and the family of regularized Newton estimators are equivalent when the regularization matrix is replaced by the square root of the inverse of the covariance matrix; regularization parameters can therefore be considered as scaling factors in the MAP formulation. Several methods for constraining the inversion of ERT data set using prior information provided by another geophysical methods or geological knowledge have been suggested (e.g. Kaipio et al. 1999; Saunders et al., 2005; Günther and Rücker, 2006; Johnson et al., 2007, 2012; Lelièvre and Oldenburg, 2009; Zhou et al., 2014; Caterina et al., 2014). Joint inversion is probably the most familiar technique (e.g. Günther and Rücker, 2006; Bouchedda et al, 2012). Geostatistical (e.g. Johnson et al., 2007; Herman et al., 2012) and structural inversion (Kaipio et al., 1999; Zhou et al., 2014) approaches are more and more used. In our case, structural information is extracted using gradient tensor in the same way as structurally inversion approach (Kaipio et al., 1999) but included in the inversion system using covariance function such as geostatistical inversion (Herman et al., 2012).

In this paper, the ERT inverse problem is solved using Bayesian MAP estimation approach such as presented in Yang and Labrecque (1998). The key point of this approach is to choose a good model covariance function that best represents the true resistivity variability within the Earth. In general, covariance functions are chosen stationary which means that their parameters (correlation length or range, variance and anisotropy) depend only on the distance between any two points in the grid. In other words, the covariance function is assumed be spatially invariant over the investigated area. It implies that the geological heterogeneities share within the study area, some similarities in size (related to the range), orientation (related to the main anisotropy

directions), and variability of the physical property (related to the variance). However, in most real cases, spatial resistivity variability is position dependent because all parameters that affect bulk resistivity such as pore water resistivity, water content, temperature and clay content vary spatially with lithology and fluid. For example, a dipping layered resistivity model has a range that is more important in the direction of the dip. However, it is generally very difficult to assess non-stationarity when considering exclusively the measured potential data and well resistivity logs alone, as the already under-determined problem sees its degrees of freedom increase even more. In our methodology, all *a priori* information such as geological knowledge, ground penetration radar or seismic reflection techniques and ERT sensitivity are used to improve the knowledge of the non-stationarity in model parameters' covariance matrix. More precisely, all additional information is introduced by allowing spatial variations of range or anisotropy or marginal variance.

A few approaches have been developed for non-stationary covariance calculation. An overview is given in Sampson (2010) and Fuglstad et al.(2015b). In the literature on geophysical inverse problems, Shamsipour et al.(2013) used the Matérn-like process convolution of Paciorek and Schervish (2006) to invert gravity data. However, the covariance matrix is generally dense, especially when range parameter is high. Hence, efficient implementation of stochastic Bayesian approach using MAP estimator becomes critical for large-scale problems and non-stationary covariance functions. Unfortunately, inversion of the covariance matrix, as well as covariance matrix multiplication, can be efficiently calculated and with small memory requirements only for isotropic, stationary and regular grids cases (e.g. Linde et al., 2006). To avoid this problem, Aune et al. (2013) proposed to work with non-stationary precision matrix to invert amplitude variation with

1
2
3
4
5
6
7
8
9
10
11
12
13
14
15
16
17
18
19
20
21
22
23
24
25
26
27
28
29
30
31
32
33
34
35
36
37
38
39
40
41
42
43
44
45
46
47
48
49
50
51
52
53
54
55
56
57
58
59
60

1
2
3
4
5
6
7
8
9
10
11
12
13
14
15
16
17
18
19
20
21
22
23
24
25
26
27
28
29
30
31
32
33
34
35
36
37
38
39
40
41
42
43
44
45
46
47
48
49
50
51
52
53
54
55
56
57
58
59
60

angle (AVA) data. In their approach, originally developed by Lindgren et al. (2011) based on the work of Whittle (1954), a Gaussian process is defined through linear stochastic partial differential equations (SPDE). The latter gives an explicit link between continuous Markov representations of the Matérn covariance and the Gaussian fields. One of the major advantages of this formulation is that the resulting precision matrix is very sparse, which enables efficient computation and reduces memory requirements for large-scale problems. In addition, non-stationarity can be easily implemented by spatially varying SPDE parameters. Matérn covariance functions are defined by their smoothness parameter ν that controls the degree of the smoothness of the resistivity field. Due to the SPDE construction (Lindgren et al., 2011), only integer and half-integer of ν are used in this paper. It is to be noted that an approximation was proposed by (D., Hale, 2013, Colorado School of Mines, C.W.P. report No. 815) to calculate the non-stationary Matérn covariance for any real value of ν , but it is not considered here. In this work, we suppose that the model parameters have a Gaussian distribution with non-stationary Matérn covariance with unknown ν . Covariance parameters are determined by considering prior information. Indeed, the more information about the desired properties of the solution is included in the inversion system, the more realistic the resulting models are (Günther and Rücker, 2006; Kim et al., 1999). In practice, useful information about the desired geological model can be obtained through well and surface data. In our case, we consider two types of prior information: structure orientations and ERT sensitivity. More precisely, the structure orientation can be extracted from ground penetrating radar or high resolution seismic reflection and included in the inversion system by spatially varying anisotropy factors. To address the fact that the data sensitivity of resistivity blocks

$$-\nabla \cdot \left(\frac{1}{\rho(x,z)} \nabla V(x,k,z) \right) - k^2 V(x,k,z) = \frac{I}{2} \delta(x-x_s, y-y_s) \text{ for } (x,z) \in \Omega; \quad \Omega = \Gamma_s \cup \Gamma_\infty$$

(1)

subject to the boundary conditions applied to $\partial\Omega = \Gamma_s \cup \Gamma_\infty$

$$\frac{1}{\rho(x,z)} \frac{\partial V}{\partial n} + \lambda V = 0 \tag{2}$$

where I is the current intensity, δ the Dirac function, k the wave number, n the outward normal and λ determines the boundary type.

The transformed potential V and its inverse v are related by

$$\begin{aligned} V(x,k,z) &= \int_0^\infty v(x,y,z) \cdot \cos(k \cdot y) dy \\ v(x,z) &= \frac{2}{\pi} \int_0^\infty V(x,y,z) \cdot \cos(k \cdot y) dk \end{aligned} \tag{3}$$

The closed domain Ω is delimited by the air–earth interface (Γ_s) and a fictitious boundary (Γ_∞). Homogeneous Neumann boundary conditions are applied at the air–earth interface ($\lambda = 0$) and homogeneous mixed boundary conditions are applied at the subsurface boundary based on the physical behaviour of the potential at a given distance r from the point source. The detailed discretization of equations (2) and (3) has been discussed in Dey and Morrison (1979) and will not be presented here.

1
2
3
4
5
6
7
8
9
10
11
12
13
14
15
16
17
18
19
20
21
22
23
24
25
26
27
28
29
30
31
32
33
34
35
36
37
38
39
40
41
42
43
44
45
46
47
48
49
50
51
52
53
54
55
56
57
58
59
60

INVERSE PROBLEM

We consider a Bayesian approach to ERT inversion using maximum *a posteriori* (MAP) estimator (Tarantola and Valette, 1982). This approach requires specifying uncertainty on data noise and prior information on the model parameters. In a Bayesian context, both are expressed as an *a priori* probability density functions that are usually, but not necessarily, considered Gaussians. The conditional *a posteriori* probability of the model parameters, given the measured data, is obtained using Bayes rule. The MAP estimator consists of giving the solution that maximizes the *a posteriori* distribution. For more details about mathematical foundations, an excellent presentation can be found in Idier (2013) and Tarantola and Valette (1982).

If we assume Gaussian distributions for model parameters and measured data, the maximization of the posterior probability density is equivalent to the minimization of the following objective function (Tarantola, 2005):

$$\phi(m) = \left\| C_d^{-\frac{1}{2}}(d - F(m)) \right\|_2^2 + \left\| C_m^{-\frac{1}{2}} \cdot (m - m_{prior}) \right\|_2^2 \tag{4}$$

where we denote the measured data as d , the *a priori* model m_{prior} , the forward modelling operator as F , and covariance matrix of data noise and model parameters as C_d and C_m , respectively.

In the most common approximation we may invoke the Tikhonov regularization (Tikhonov and Arsenin, 1977), and replace the square root of the inverse of the model covariance matrix by the regularization matrix R :

$$\phi(m) = \left\| W_d(d - F(m)) \right\|_2^2 + \beta \left\| R(m - m_{ref}) \right\|_2^2 \tag{5}$$

1
2
3
4
5
6
7
8
9
10
11
12
13
14
15
16
17
18
19
20
21
22
23
24
25
26
27
28
29
30
31
32
33
34
35
36
37
38
39
40
41
42
43
44
45
46
47
48
49
50
51
52
53
54
55
56
57
58
59
60

In this paper, we used the following regularization matrix (Pidlisecky et al., 2007) when comparing our algorithm to smooth inversion:

$$\mathbf{R} = l_x \mathbf{D}_x + l_z \mathbf{D}_z + l_s \mathbf{I},$$

where:

\mathbf{D}_x : first derivative matrix in x direction

\mathbf{D}_z : first derivative matrix in z direction

\mathbf{I} : identity matrix

l_x, l_z : smoothing weighting factors in x and z direction respectively

l_s : smallness or closeness weighting factor.

The only difference is the regularization parameter β that is not present in Bayesian formulation. Note that some authors (e.g. Linde et al., 2006) replaced the regularization matrix in (5) by the precision matrix and used the term ‘stochastic regularization’. Interface or boundary constraints can be implemented by weighting the regularisation matrix \mathbf{R} . The weighting matrix contains small weights at the position of interfaces, and weights of one otherwise. When applied to the regularization matrix \mathbf{R} , this results in sharp gradients at these positions. In other words, the model is smoothed by blocks.

The minimization of equation (4) using a Gauss-Newton algorithm gives the following update equation:

$$m_{i+1} = m_i + s \Delta m_i, \text{ with}$$

$$\Delta m_i = (J^T C_d^{-1} J + C_m^{-1})^{-1} (J^T C_d^{-1} (d - F(m_i)) - C_m^{-1} (m_i - m_{ref})) \quad (6)$$

Where i refers to the i^{th} iteration and s is step length calculated using quadratic line search (Pidlisecky et al., 2007). Note that the regularization parameter can be interpreted in stochastic inversion as a scaling factor applied to the variance.

MATÉRN PRECISION MATRIX

The Matérn isotropic covariance function $Cov(h)$ is given by (Handcock and Stein, 1993; Stein, 1999)

$$Cov(\mathbf{h}) = \frac{\delta^2}{2^{v-1}\Gamma(v)} (\kappa\|\mathbf{h}\|)^v K_v(\kappa\|\mathbf{h}\|); \quad \mathbf{h} \in \mathbb{R}^n, \quad (7)$$

where \mathbf{h} is the separation distance between two location blocks, n is dimension of the field, K_v is a modified Bessel function of the second kind of order v (Abramowitz and Stegun, 1972), Γ is the gamma function, κ is the spatial scaling parameter related to the range which measures how quickly the correlations decay with distance, and v is the smoothness or shape parameter. The later controls the degree of smoothness of the spatial process. When v is small, the resistivity distribution tends to be rough, and the opposite occurs when it is large. Because there is no simple relationship between the range r and κ , we used the same empirically derived formula as (Lindgren et al., 2011), that is $r = \sqrt{8} v/\kappa$, corresponding to correlations near 0.1 at the distance r , for all v . The marginal variance δ^2 is given by

$$\delta^2 = \frac{\Gamma(v)}{(4\pi)^{d/2}\Gamma(v+n/2)\kappa^{2v}} \quad (8)$$

The Matérn covariance function is widely used in geostatistics and in many other geoscience fields (Minasny and McBratney, 2005). By varying the smoothness parameter v , it is possible to retrieve or approximate a few well-known covariance functions, as

1
2
3
4
5
6
7
8
9
10
11
12
13
14
15
16
17
18
19
20
21
22
23
24
25
26
27
28
29
30
31
32
33
34
35
36
37
38
39
40
41
42
43
44
45
46
47
48
49
50
51
52
53
54
55
56
57
58
59
60

presented in Table 1. It can be also linked to smooth regularisation operator as shown by Maurer et al. (1998).

The idea of calculating a random Gaussian field with a Matérn covariance structure with SPDE was firstly introduced by Whittle (1954). More recently, Lindgren et al. (2011) extended Whittle's work by discretizing the SPDE with finite-elements, which gives an efficient calculation of the Matérn precision matrix for any integer and half-integer ν value. The SPDE is given by (Whittle, 1963, 1954):

$$(\kappa^2 - \Delta)^{\alpha/2}(\tau x(\mathbf{u})) = W(\mathbf{u}), \mathbf{u} \in \mathbb{R}^n, \alpha = \nu + \frac{n}{2}, \kappa > 0, \nu > 0 \quad (9)$$

where $x(\mathbf{u})$ is a random Gaussian field at location \mathbf{u} , $W(\mathbf{u})$ is Gaussian white noise with unit variance, Δ is the Laplace operator, and $\alpha = \nu + n/2$, n is the dimension of the field.

The discretization of equation (9) can be done using any numerical methods, such as finite-elements (Lindgren et al., 2011), finite-volumes (Fuglstad et al., 2015a) or finite-differences (Aune et al., 2013). In this paper, we used the formulation of Lindgren et al. (2011) where the solution is obtained using finite-elements with linear basis functions. We chose not to present detailed derivations because they are quite involved and can be found in Lindgren and Rue (2007, Lund University Publications, Preprints in Mathematical Sciences No. 5). However, when the form of the discretized SPDE has been derived as an expression of the coefficients in the SPDE and the grid for $\alpha = 1$ ($\nu = 0$) and 2 ($\nu = 1$) (see appendix A), the Matérn precision matrix for any integer $\alpha > 2$ is obtained using the recursive form of the SPDE (Lindgren et al., 2011). Half-integer values of α or ν are obtained using Taylor approximation the precision matrix as described in author's discussion response in Lindgren et al. (2011).

A covariance function is called isotropic when it is invariant in all directions at any point of the grid. Geometrical anisotropy occurs when the range is directional depend. For simplicity, we refer to geometrical anisotropy as anisotropy in all the text. To include anisotropy into the Matérn precision matrix, a tensor field \mathbf{H} (2×2) is introduced in equation (9) such that

$$(\kappa^2 - \nabla \cdot \mathbf{H} \nabla)^{\alpha/2} (\tau \mathbf{x}(u)) = \mathbf{W}(u), u \in \mathbb{R}^n, \alpha = \nu + \frac{d}{2}, \kappa > 0, \nu > 0, \quad (10)$$

where \mathbf{H} can be parameterized as proposed by (Fuglstad et al., 2015a)

$$\mathbf{H} = \gamma \mathbf{I} + \eta \mathbf{g} \mathbf{g}^T,$$

with $\mathbf{g} = [\cos(\theta) \sin(\theta)]^T$, $\gamma > 0$ and $\eta > 0$. The angle θ indicates how much the coordinate system has been rotated in clockwise direction. $\gamma > 0$ ensures that \mathbf{H} is strictly a definite positive matrix. The marginal variance is now given by (Fuglstad et al., 2015a)

$$\delta^2 = \frac{\Gamma(\nu)}{\Gamma(\alpha) (4\pi)^{d/2} \kappa^{2\nu} \tau^2 \sqrt{\lambda_1 \lambda_2}} \quad (11)$$

where $\lambda_1 = \gamma + \eta$ and $\lambda_2 = \gamma$ are the eigenvalues of matrix \mathbf{H} .

The eigenvectors of \mathbf{H} define the two principal directions of correlation ellipse and $\sqrt{\lambda_1}/\kappa$ and $\sqrt{\lambda_2}/\kappa$ can be considered as a measure of correlation lengths in these principal directions.

In (10), the statistical properties of the random field are characterized by the SPDE rather than by the Matérn covariance function (equation (7)). In such case, non-stationarity can be easily handled by allowing spatial variation of κ , τ and \mathbf{H} . In other words, nonstationary anisotropy is defined as ellipses around each point that describe locally a change of distances such that correlation lengths are different in different directions.

Precision matrix parameters determination

From equation (10), the Matérn precision matrix can be defined using four control parameters ($\nu, \tau, \kappa, \mathbf{H}$) which give a great flexibility to handle all *a priori* information in the inverse system. As previously mentioned, we consider only integer or half-integer values for the smoothness parameter ν of the stochastic partial differential equation parameter α (Lindgren et al., 2011). In the 2-D case ($d=2$), the precision Matérn matrix can be calculated for $\nu = 1/2, 1, 3/2, 2, 5/2, 3, 7/2, 4, \dots$. Note that for $\nu = 0$, the random fields that are solutions of the stochastic differential equation (9) don't have a Matérn covariance. For a fixed value of smoothness parameter ν , the spatial scaling parameter κ controls the spatial correlation length (range). The marginal variance as described by equation (11) depends on all parameters ($\nu, \tau, \kappa, \mathbf{H}$). However, if ν and κ are fixed, τ can be used to control the variance.

In practice, covariance parameters can be determined by variogram modelling of resistivity well logs data (Linde et al, 2006; Caterina et al., 2014). However, well logs data are generally not available or only available at some sparse locations of resistivity profile. In this case, geological knowledge can be used as a guideline to choose the range and the variance. Another solution is to use V-V plot as proposed by Asli et al. (1999) to calculate the control parameter from data covariance. However, this approach was developed for linear inverse problem such as gravity inversion and needs covariance matrix multiplication with sensitivity matrix, which is not practical for large-scale problems.

1
2
3
4
5
6
7
8
9
10
11
12
13
14
15
16
17
18
19
20
21
22
23
24
25
26
27
28
29
30
31
32
33
34
35
36
37
38
39
40
41
42
43
44
45
46
47
48
49
50
51
52
53
54
55
56
57
58
59
60

In our methodology, we suppose first that ν is unknown and can take any integer or half-integer values. In practice, the maximum value considered in this work is 4. We believe that inversion with a few values of ν , as ν is smoothing factor, can give an idea about features in the resistivity model that are well constrained by the data. As previously mentioned, κ and τ are function of range and variance, but the latter are not known *a priori*. We circumvent the problem by relying on the experimental variogram of a model obtained after smooth resistivity inversion to determine the range r . The variance is taken as the square of the maximum resistivity value of smooth inversion. The effect of such choices will be studied in the first synthetic example.

To introduce additional information using Matérn precision matrix, two types of non-stationary parameters were used. First, we considered spatial variation of the range parameter. In fact, as the sensitivity of ERT is inversely proportional to the distance from the electrodes, the resolution of deeper blocks should be lower than shallower blocks when surface measurements alone are input in the inversion. To take into account the decreasing resolution with increasing depth, Loke (M.H, Loke, 2015, Geotomo Software, Tutorial Notes) proposed for example to increase the size of blocks with depth. In this study, we chose to use the same block size on the entire region of interest, but we increased the correlation between blocks with depth by increasing the range parameter. It is important to note that the resistivity variability that can be assessed by ERT is scale dependent. In other words, the resistivity variability that can be seen by the smallest electrode separation measurements is different from those of largest electrode separation measurements. Increasing correlation length with the depth will reduce small scale variability that is not assessed by largest electrode separation. Generally, structural

information (layering, dip, structures directions) can be obtained from GPR or shallow seismic refraction/reflection. This information can be easily introduced in inversion system using non-stationary anisotropy that encodes it as correlation ellipse at each grid point

ALGORITHM DESCRIPTION

The proposed approach can be divided in five main steps:

1. Smooth inversion.
2. Determination of the range r and the variance δ^2 from smooth resistivity model.
3. If GPR or seismic reflection or geological information are available estimate \mathbf{H} for each block using the structure tensor.
else
consider spatial variation of the range parameter.
4. Select ν and calculate τ and κ from r and δ^2
5. Perform Bayesian inversion.

The algorithm is stopped when the rms is bellow the target misfit of 1. In order to introduce GPR structural information into the stochastic inversion system, structure orientations should be extracted from GPR or seismic reflection image. In our case, we used the structure tensor that was initially introduced for corner detection (Förstner, 1986; Harris and Stephens, 1988) and oriented texture analysis (Kass and Witkin, 1987). It consists of a field of symmetric positive matrices calculated from gradient tensor convolved with a Gaussian filter. It encodes the local orientation and anisotropy of an image.

SYNTHETIC STUDY

The objectives of this section are to present the effect of the choice of parameters ν , τ and κ , and to highlight the flexibility and limitations of using non-stationary Matérn precision matrix for incorporating available information in the inversion system. Three synthetic models are used for that purpose. For all experiments, a 3% Gaussian noise was added to the data. The discretization of the region of interest was performed using regular grids of 0.25m x 0.25m and 0.5m x 0.5m for forward modelling and inverse problems respectively. A homogeneous model with a resistivity equal to the median value of apparent resistivity values was chosen as the initial model and *a priori* model for ERT data inversion. Note that when we refer to the layered model, the last layer has a semi-infinite extension and the term ‘interface’ means the border forming a common boundary between two media of different resistivities. Note that all inversions presented in the synthetic study were converged to rms below the target misfit of 1.

Synthetic model 1

The first resistivity model, called Model 1, consists of three layers with a conductive infill within the deeper layer that aims at resembling a clay lens in sedimentary environment. The measurements are simulated using a surface dipole-dipole protocol with 41 electrodes with a 1 m electrode spacing. Note that the dipole-dipole array is most suitable for vertical structure delineation and therefore not so efficient in resolving the resistivity contrast between the second layer (10 ohm.m) and the conductive infill. Before starting stochastic inversion, we will present first the results of smooth deterministic inversion in order to compare our approach with the conventional one.

1
2
3
4
5
6
7
8
9
10
11
12
13
14
15
16
17
18
19
20
21
22
23
24
25
26
27
28
29
30
31
32
33
34
35
36
37
38
39
40
41
42
43
44
45
46
47
48
49
50
51
52
53
54
55
56
57
58
59
60

1
2
3
4
5
6
7
8
9
10
11
12
13
14
15
16
17
18
19
20
21
22
23
24
25
26
27
28
29
30
31
32
33
34
35
36
37
38
39
40
41
42
43
44
45
46
47
48
49
50
51
52
53
54
55
56
57
58
59
60

Figure 1b shows the smooth inversion result without any constraint. As expected, the second layer, between 1 and 2 m depths, is not well resolved. It appears as a few localized conductive zones with resistivity values around 10 ohm.m. In addition, it is not possible to separate the conductive infill at 1 ohm.m from the second layer of resistivity of 10 ohm.m. Again, this can be explained by the sensitivity of the dipole-dipole array, which is not suitable to image horizontal structures. The top and the bottom of the conductive infill are not well defined but their extensions in x direction are well retrieved. To improve inversion results and reduce the effect of low sensitivity effect of dipole-dipole array to horizontal structures, additional constraints should be used.

First, we suppose that the layer interfaces at 1 m and 2 m are known, for example from ground-penetrating-radar or seismic data. Figures 1c and 1d show inversion results when interfaces are imposed at 1 m depth and both 1 m and 2 m depths, respectively. We can observe that in both cases the shape of the conductive infill is not improved. However, the second layer is better delimited although its resistivity shows a few lateral variations. To reduce the effect of dipole-dipole array sensitivity that “tries” to incorporate more vertical resistivity variations, l_z was set to 0.2, much lower than l_x which was set to 1. As the smoothness in the horizontal direction is stronger than in the vertical direction, layered structures are encouraged by the inversion. As shown in Fig. 1(e), the inversion result is considerably improved. The shape of the conductive infill is better defined but its extension in z appears more exaggerated than in reality. The shape of the conductive infill is better retrieved when all constraints are applied, as shown in Fig. 1f. A few artifacts are nevertheless introduced in the second layer. It is also interesting to

note that all inversion runs cannot separate clearly the second layer and the conductive infill.

For stochastic inversion, we need to infer three parameters (ν , τ and κ). In the following tests, the smoothing parameter ν takes the values of 1, 1.5, 2, 3 and 4. As described above in the section presenting the precision matrix parameters determination, κ and τ are estimated from smooth inversion results. The experimental isotropic variogram obtained using smooth inversion results (Figure 1b) is shown in Figure 2. We can observe that the sill is reached at approximately 8 m. The standard deviation is chosen to be 100.

To study the effect of the variation of the range on inversion result, κ and the standard deviation were fixed to 2 and 100, respectively, and the range was varied from 2 m to 20 m. Figure 3 shows inversion results for range values r of 2 m, 4 m, 6 m, 8 m, 10 m and 20 m. It can be observed that when the range is greatly underestimated (2 m), a few artefacts appear in resistivity image (Fig 3a), but when the range is overestimated the resulting model is highly smoothed (Figure 3f). When it is equal to 4 m, the shape of conductive infill is better defined but the second layer appears as a few conductive zones. Increasing the value of the range improves the definition of the second layer but the conductive infill appears slightly smeared. Note that the results obtained using range values between 4 m and 10 m are quite similar. Hence, it is not critical to estimate precisely the range, as inversion results are satisfactory for a rather wide bracket of values. The same behaviour has already been observed in several papers using covariance-based inversion (Yeh and Liu, 2000, Hansen et al. 2006, Hermans et al. 2012,

1
2
3
4
5
6
7
8
9
10
11
12
13
14
15
16
17
18
19
20
21
22
23
24
25
26
27
28
29
30
31
32
33
34
35
36
37
38
39
40
41
42
43
44
45
46
47
48
49
50
51
52
53
54
55
56
57
58
59
60

Hermans et al., 2016). The range value of 8m obtained from smooth inversion appears a good candidate for stochastic inversion.

In order to explore the effect of the standard deviation on inversion, the range parameter was fixed to 8 m and the standard deviation was varied from 10 Ω .m to 1000 Ω .m. As shown in the Figure 4, the resistivity of the recovered models is not highly affected by the variations of standard deviation. This is due to the fact that the resistivity values are principally controlled by the data rather than the covariance term. However, when the standard deviation is too small the resistivity seems to be slightly underestimated. In contrary, when the standard deviation is over-estimated (Figure 4d), there is barely an effect on the inversion results. As shown by Day-Lewis and Lane (2004) the statistical parameters extracted from a tomogram are biased by the regularisation. Consequently, as the standard deviation determined from smooth inversion is necessarily underestimated (due to smoothing), we propose to use the maximum value of smooth resistivity.

In conclusion, Bayesian inversion is more affected by the range than the variance. Without any borehole information, the range can be inferred from experimental variograms computed on smooth resistivity inversion images. However, as the inverted image is smooth, the range will be overestimated.

To mimic smooth inversion with horizontal anisotropic smoothing (Figure 1e), Bayesian inversion was carried out using covariance matrix with horizontal anisotropy by choosing the rotation matrix \mathbf{g} equal to (1, 0). Inversion results for different ν are shown

1
2
3
4
5
6
7
8
9
10
11
12
13
14
15
16
17
18
19
20
21
22
23
24
25
26
27
28
29
30
31
32
33
34
35
36
37
38
39
40
41
42
43
44
45
46
47
48
49
50
51
52
53
54
55
56
57
58
59
60

in the Figure 5. It appears clearly that the inversion results are greatly improved by introducing this information. Generally, all interfaces are well localized. The combination of horizontal anisotropy and the high sensitivity of the dipole-dipole array to vertical structures allows a very nice definition of the extensions of the conductive infill. The resistivity and continuity of the bedrock are better estimated for ν values of 3 and 4. This can be explained by the fact that when ν is high the smoothing effect is more pronounced which produces less resistivity variations and better estimation of bedrock resistivity.

Finally, to reduce the effect of high sensitivity of the dipole-dipole array that tries to generate limited size structures rather than continuous layer in the inversion (see Figure 3 and 4), we introduce a spatially-varying range that increases smoothly the correlation between blocks as the depth increases. As the spatial scaling parameter κ is inversely proportional to the range parameter r , we used the following

$$\kappa_i = \max \left\{ \kappa_0 \left(\frac{F(z_i)}{\max(F(z_i))} \right), \kappa_{min} \right\}; \text{ with } F(z) = \frac{1}{z^\gamma}, i = 1, \dots N. \tag{12}$$

Where z is the depth of resistivity block i , N is the number of blocks, γ is a constant that controls the degree of variations of $F(z)$ and κ_0, κ_{min} are respectively the spatial scaling parameter values at surface and its minimum value corresponding to the maximum range.

For inversions performed in this work, κ_0 is selected on the basis that the range for surface blocks corresponds to the shortest distance between electrodes (here 1m). Inversion results with non-stationary correlation based on equation (12) are presented in the Figure 6. It is clear that the results are improved in comparison to smooth and

1
2
3
4 isotropic Bayesian inversion. We observe that the second layer is well delimited but not as
5 well as in the case of Bayesian or smooth anisotropic inversion (Figure 5). This can be
6 explained by isotropic range. However, the conductive infill is better retrieved in all
7 cases. In addition, the resistive bedrock is better defined as ν increases. In fact, the
8 smoothing effect increases with increasing ν , which allows retrieving a more
9 homogeneous bedrock.
10

11 Synthetic model 2

12 The second model, shown in Figure 7, consists of a conductive dyke crossing five
13 layers at 45 degrees. The resistivity of the layers varies between 50 ohm.m and 500
14 ohm.m, and the latter is located in the center of the panel, where the ERT sensitivity is
15 the lowest. A bipole-bipole crosshole survey with additional surface electrodes (Binley
16 and Kemna, 2005) is simulated. Based on smooth inversion resistivity, r and δ were
17 chosen to be 3 and 1000, respectively.
18

19 Figure 7 shows the results obtained with smooth inversion as well as Bayesian
20 inversion with stationary covariance model. We can observe that the resistivity images
21 contain a few artefacts, the conductive dyke is not well defined and the fourth layer
22 between 4 m and 6 m depths appears more conductive and in some cases not well
23 delimited. It is interesting to note that Bayesian inversion with $\nu=1$ gives the best result.
24 More precisely, the conductive dyke is clearly distinguishable and the limits of the fourth
25 layer are well determined (Fig. 7(c)). When ν increases, the resulting resistivity models
26 are smoother, and the conductive dyke disappears from the images whereas the fourth
27
28
29
30
31
32
33
34
35
36
37
38
39
40
41
42
43
44
45
46
47
48
49
50
51
52
53
54
55
56
57
58
59
60

layer appears larger. As ν controls the smoothness of the resistivity image, the thin dyke is better characterised by the smallest value of ν .

In order to demonstrate that our inversion with non-stationary anisotropy can successfully assimilate any knowledge of the geological and stratigraphic structures, we perform several experiments supplying various combinations of zones and preferential directions for the dyke model. We choose $\mathbf{g}=(- 1/2, 1/2)^T$ in the dyke region and $\mathbf{g}=(1,0)^T$ elsewhere for the first three tests. Inversion results are presented in Figure 8. In the three first tests, the *a priori* model was chosen to be $(\log (85))$, $\log(1000)$ and $\log(10000)$ respectively. As shown in Figures 8b to 8d, the *a priori* model doesn't have much effect on the final inversion results. This can be explained by the combination of three factors: (1) a good *a priori* information introduced in non-stationary anisotropy, (2) a large standard deviation and (3) the resolution of cross-borehole measurements. In the second experiment, the dip of the dyke was imposed to the whole domain by chosen $\mathbf{g}=(- 1/2, 1/2)^T$ constant on all grid cells. Inversion result shows that the dyke position is well retrieved (Figure 8e). However some artifacts are apparent and the layer between 4m and 6m seems to have a dip. Finally, in the last test the anisotropy is defined by supposing vertical dyke located in the middle of the panel. Inversion result is presented in the Figure 8f. Surprisingly, with wrong information the dyke can be seen but its shape cannot be retrieved. Note that, in all cases, the estimated resistivity models were improved in the comparison to isotropic case.

1
2
3
4
5
6
7
8
9
10
11
12
13
14
15
16
17
18
19
20
21
22
23
24
25
26
27
28
29
30
31
32
33
34
35
36
37
38
39
40
41
42
43
44
45
46
47
48
49
50
51
52
53
54
55
56
57
58
59
60

INVERSION OF FIELD DATA

The objective of this section is to demonstrate the effectiveness and flexibility of the proposed approach to invert real resistivity data. The structural constraints on the covariance come from a ground penetrating radar survey made at the same location than the ERT profile. The study area is located in St-Lambert-de-Lauzon, Québec, Canada (Figure 9). In 2008, a hydro-geophysical study was conducted in order to understand groundwater flow and contaminant transport in the shallow granular aquifer of the Beaurivage river sub-watershed. The latter encloses a decommissioned sanitary landfill emitting a leachate plume managed by natural attenuation (Paradis et al., 2014, Tremblay et al., 2014). The granular aquifer consists of 10 to 15 m thick heterogeneous sand layer over discontinuous till aquitard and interbedded with thin intercalated silty to clayey lenses. The bedrock aquifer is composed of fractured shale and sandstone. The water table is close to the surface at approximately 0.2 m to 2 m depth. A more detailed description can be found in (Gloaguen et al., 2012; Paradis et al., 2014; Tremblay et al., 2013). ERT, cone penetrating test (CPT) and ground penetrating radar (GPR) were carried out in order to characterize the aquifer geometry and to improve forecasting of mass transport. In the following, we will present the results of one survey line located in the North of the study area where all the data are collocated (Figure 9).

2D ERT data acquisition was performed using an automatic resistivity imaging system with 96 electrodes and 2 m spacing. The dipole-dipole array protocol defined on a 190 m long baseline was extended to 490 m long profile using a roll-along technique. In

total, 8394 electric potential differences were recorded. GPR data was acquired using a 100 Mhz antennas. It was processed by applying a dewow filter, a spreading gain function, a bandpass filter (40–110 MHz) and Kirchoff migration (Cassidy, 2009). Time to depth conversion was performed using a constant velocity value of 0.07 m/ns obtained from CPT data and hyperbola fitting on diffractions on larger blocks in the top of the till. It is important to note that the maximum layer dip is generally less than 5 % except at the end of GPR profile where the dip is approximately 10%. It appears visually more important in the GPR image (Figure 10c) due to a vertical to horizontal scale ratio of 1/10.

The GPR image is shown in the Figure 10c. The base of sandy aquifer can be easily identified as the last strong reflection, which is located at depth between 5 m and 12 m. Its stratification, typical of coastal environments, can be also observed and gives an idea of depositional modes. More details can be found in Paradis et al. (2014). The till, which is the aquitard, is characterized by the presence of boulders or cobbles that generates numerous hyperbolas at positions $X=150$ m to $X=250$ m and $X=400$ m to $X=475$ m. Two attenuated zones can be identified between $X=0$ m to $X=150$ m and $X=275$ m to $X=350$ m. Chemical analysis of pore water at these places show high water conductivities due to the sanitary landfill leachate plume.

Smooth inversion results of ERT data are presented in Figure 10. In order to show structural similarity between GPR and resistivity images, a few interfaces extracted from GPR image are plotted (white lines) on all resistivity inversion images. For isotropic smoothing factors, the resistivity image presents a good structural similarity with GPR profile between 0 to 5 m depths, as shown in Figure 10a. This can be explained by the

1
2
3
4
5
6
7
8
9
10
11
12
13
14
15
16
17
18
19
20
21
22
23
24
25
26
27
28
29
30
31
32
33
34
35
36
37
38
39
40
41
42
43
44
45
46
47
48
49
50
51
52
53
54
55
56
57
58
59
60

1
2
3
4
5
6
7
8
9
10
11
12
13
14
15
16
17
18
19
20
21
22
23
24
25
26
27
28
29
30
31
32
33
34
35
36
37
38
39
40
41
42
43
44
45
46
47
48
49
50
51
52
53
54
55
56
57
58
59
60

fact that this zone is well constrained by ERT data. Below 5 m depth, a few conductive circular zones appear on the resistivity image, which are principally due to the sensitivity of dipole-dipole array. In addition, the base of sandy aquifer is not well as defined as the GPR section shows. To improve inversion results, an anisotropic smoothing factor was used ($l_z/l_x=5$) to favor horizontal structures. Inversion results are shown in Figure 10b. As expected, structural similarity between GPR and resistivity images is considerably enhanced. The layered structure of sandy aquifer is more pronounced and the base of the aquifer at positions $X=0$ to $X=100$ m is the same as in the GPR section.

In order to introduce GPR structural information into the Bayesian inversion system, structure orientations were extracted from GPR image using the structure tensor as described in algorithm description section. Note that the structure orientations are first calculated on the high resolution GPR image. After, the mean value on each resistivity block support (1 m^2) is used to construct the structural orientation field \mathbf{g} for each resistivity block of the grid. Figure 11a shows the structure orientation field as extracted from the GPR image.

Inversion results using the non-stationary anisotropic Matérn precision matrix based on GPR information are presented in Figure 11. The structural similarity between ERT and GPR images is now highly enhanced. Between $X=0$ to $X=120$ m and $X=400$ m to $X=475$ m positions, the bedrock interface is continuous showing a high resistivity. In the contrary, the interface with the bedrock between $X=100$ m and $X=400$ m seems to be discontinuous with the base of sandy aquifer. This might be due to the presence of fractures generating a strong anisotropy. It is interesting to note that the structure orientations captured below the sandy aquifer interface in leachate zones don't affect

1
2
3
4
5
6
7
8
9
10
11
12
13
14
15
16
17
18
19
20
21
22
23
24
25
26
27
28
29
30
31
32
33
34
35
36
37
38
39
40
41
42
43
44
45
46
47
48
49
50
51
52
53
54
55
56
57
58
59
60

inversion results. It is clear from GPR section and resistivity images that structural information at these locations are not compatible. In other words, in high sensitivity zones where the inversion result is better constrained by measured data, structural constraints act as soft constraints. Resistivity model in these regions is controlled by the data rather than structural information that are not compatible with resistivity variability.

CONCLUSION

Structure orientation obtained from GPR image can be efficiently incorporated in constrained Bayesian inversion using nonstationary Matérn covariances. The latter are constructed using a finite-element discretization of the SPDE. In such formulation, nonstationarity of anisotropy and range parameters are easily implemented by spatially varying the SPDE parameters. Synthetic data tests show that inversions are robust to misdetermination of the variance, ranges and prior model. In practice, these parameters are estimated on the basis of smooth inversion results. When no structural prior information is available, we proposed to constraint the inversion by heuristically increasing the range with increasing depth. Our results indicate that the proposed approach can perform better than isotropic covariance based inversion. Further works should be realised to explore other functions for spatially varying range. Finally, structurally Bayesian constrained inversion was applied to characterize sandy aquifer contaminated by sanitary landfill leachate plume. GPR image serves to extract orientation structures that were included in inversion system using nonstationary anisotropic covariance. The introduction of this information gives a resistivity model that is more

compatible with the aquifer structure. The proposed approach can be easily extended to the 3D case and to unstructured meshes.

APPENDIX A

The discrete approximation of continuous Gaussian field $x(u)$ can be constructed using basis functions, $\{\psi_k\}$, and weights, $\{w_k\}$,

$$x(u) = \sum_k \psi_k(u) w_k \tag{A-1}$$

A stochastic weak formulation of the SPDE states that

$$[\langle \phi_k, (\kappa^2 - \Delta)^{\alpha/2}(x(u)) \rangle]_{k=1, \dots, m} = [\langle \phi_k, W(u) \rangle]_{k=1, \dots, m} \tag{A-2}$$

for each set of test functions $\{\phi_k\}$.

Replacing $x(u)$ in (A-2) by (A-1) gives

$$[\langle \phi_i, (\kappa^2 - \Delta)^{\alpha/2} \psi_j \rangle]_{i,j} = [\langle \phi_k, W(u) \rangle]_k \tag{A-3}$$

Let's study the case of $\alpha=2$ and $\phi_i = \psi_i$,

$$\kappa^2 [\langle \psi_i, \psi_j \rangle]_{i,j} + [\langle \psi_j, -\Delta \psi_j \rangle]_{i,j} = [\langle \psi_k, W(u) \rangle]_k \tag{A-4}$$

if we define:

$$\begin{aligned} L_{i,j} &= \langle \psi_i, \psi_j \rangle \\ G_{i,j} &= \langle \psi_j, -\Delta \psi_j \rangle \\ K_{i,j} &= \langle \psi_i, (\kappa^2 - \Delta) \psi_j \rangle = \kappa^2 L_{i,j} + G_{i,j} \end{aligned}$$

From equation (A-4), a weak solution to SPDE is given by $\mathbf{A}^{-1} \mathbf{w} \sim \mathbf{N}(\mathbf{0}, \mathbf{L})$ where $\mathbf{A} = \kappa^2 \mathbf{L} + \mathbf{G}$. Hence, the Matérn precision matrix of the weights, \mathbf{w} , is given by

$$\mathbf{C}_{\mathbf{m}(\alpha=2)}^{-1} = (\kappa^2 \mathbf{L} + \mathbf{G})^T \mathbf{L}^{-1} (\kappa^2 \mathbf{L} + \mathbf{G}) = \mathbf{K}^T \mathbf{L}^{-1} \mathbf{K} \tag{A-5}$$

Choosing test functions equal to the linear operator applied to the basis functions
 ($\phi_i = (\kappa^2 - \Delta)^{\alpha/2} \psi_j$) leads the Matérn precision matrix for $\alpha=1$

$$\mathbf{C}_{m(\alpha=1)}^{-1} = (\kappa^2 \mathbf{L} + \mathbf{G}) = \mathbf{K} \tag{A-6}$$

Using A-2 and having precision matrix for $\alpha=1$ and $\alpha=2$, the Matérn precision matrix for any integer α greater than 2 can be calculated using the following recursive equation:

$$\mathbf{C}_{m(\alpha=n)}^{-1} = \mathbf{K}^T \mathbf{L}^{-1} \mathbf{C}_{m(\alpha=n-2)}^{-1} \mathbf{L}^{-1} \mathbf{K}, \quad n = 3, 4, \dots \tag{A-7}$$

Lindgren et al. (2011) proposed to use a piecewise linear basis (finite elements) which give only neighbouring basis functions overlap. Consequently, L and G are sparse matrix. However, the inverse of L is not sparse. To overcome this problem, L is replaced with diagonal elements $L_{i,j} = \langle \psi_i, 1 \rangle$. As shown by Lindgren et al. (2011) the resulting approximation error is small.

Acknowledgments

This work was supported by the Canada Research Chair in Assimilation of Geological and Geophysical Data for Stochastic Geological Modelling and FQRNT grant to E. Gloaguen and Carbon Management Canada, CMC-NCE, grant C394 to B. Giroux.

REFERENCES

Abramowitz, M., and I.A., Stegun, 1972, Hadbook of Mathematical Functions with Formulas, Graphs, and Mathematical Tables: Dover.

1
2
3
4
5
6
7
8
9
10
11
12
13
14
15
16
17
18
19
20
21
22
23
24
25
26
27
28
29
30
31
32
33
34
35
36
37
38
39
40
41
42
43
44
45
46
47
48
49
50
51
52
53
54
55
56
57
58
59
60

1
2
3
4
5
6
7
8
9
10
11
12
13
14
15
16
17
18
19
20
21
22
23
24
25
26
27
28
29
30
31
32
33
34
35
36
37
38
39
40
41
42
43
44
45
46
47
48
49
50
51
52
53
54
55
56
57
58
59
60

Asli, M., D. Marcotte, and M. Chouteau, 2000, Direct inversion of gravity data by cokriging, in Kleingeld and Krige, eds., 6th International Geostatistics Congress: Geostatistical Association of South Africa, 64–73.

Aune, E., Eidsvik, J., and Ursin, B., 2013, Three-dimensional non-stationary and non-linear isotropic AVA inversion: *Geophysical Journal International*. **194**, 787–803. doi:10.1093/gji/ggt127

Binley, A.M., and Kemna, A., 2005, Electrical methods., *in*: Rubin, Y., Hubbard, S.S. eds., *Hydrogeophysics: Water Science and Technology Library*. Springer, 129–156.

Bouchedda, A., Chouteau M., Binley, A. & Giroux, B., 2012. 2-D joint structural inversion of cross-hole electrical resistance and ground penetrating radar data: *Journal of Applied Geophysics*, **78**, 52-67.

Caterina D., Hermans T. and Nguyen F. 2014, Case studies of incorporation of prior information in electrical resistivity tomography: comparison of different approaches: *Near Surface Geophysics*, **12**, 451-465.

Day-Lewis F. and Lane J., 2004, Assessing the resolution-dependent utility of tomograms for geostatistics: *Geophysical Research Letters*, **31**, L07503.

Dey, A., and Morrison, H.F., 1979, Resistivity Modelling For Arbitrarily Shaped Two-Dimensional Structures: *Geophysical Prospecting*. **27**. 106–136. doi:10.1111/j.1365-2478.1979.tb00961.x

Doetsch J., Linde N., Pessognelli M., Green A.G. and Gunther T., 2012, Constraining 3-D electrical resistance tomography with GPR reflection data for improved aquifer characterization: *Journal of Applied Geophysics*, **78**, 68-76.

1
2
3
4 Förstner, W., 1986, A feature based correspondence algorithm for image matching.
5
6 International Archives of the Photogrammetry: Remote Sensing and Spatial Information
7
8 Sciences, **26**. 150–166.

9
10 Friedel, S., 2003, Resolution, stability and efficiency of resistivity tomography estimated
11
12 from a generalized inverse approach: Geophysical Journal International. **153**. 305–316.
13
14 doi:10.1046/j.1365-246X.2003.01890.x

15
16 Fuglstad, G. A., Lindgren, F., Simpson, D., and H., Rue, 2015a, Exploring a New Class
17
18 of Non-stationary Spatial Gaussian Random Fields with Varying Local Anisotropy:
19
20 Statistica Sinica. **25**. 115–133.

21
22 Fuglstad, G. A., Simpson, D., Lindgren, F., and H., Rue, 2015b, Does non-stationary
23
24 spatial data always require non-stationary random fields? Spatial statistics, 14, 505-531.

25
26 Gloaguen, E., Lefebvre, R., Ballard, J.-M., Paradis, D., Tremblay, L., and Y., Michaud,
27
28 2012, Inference of the two dimensional GPR velocity field using collocated cokriging of
29
30 Direct Push permittivity and conductivity logs and GPR profiles: Journal of Applied
31
32 GEOPHYSICS. **78**, 94–101. doi:10.1016/j.jappgeo.2011.10.015

33
34 Günther, T., and C., Rücker, 2006, A general approach for introducing information into
35
36 inversion and examples from dc resistivity inversion : Near Surface Conference &
37
38 Exhibition, EAGE, Extended Abstract. P039.

39
40 Hancock, M.S., and M.L. Stein, 1993, A Bayesian Analysis of Kriging: Technometrics,
41
42 **35**, 403–410. doi:10.2307/1270273.

43
44 Hansen T.M., Journel A.G., Tarantola A. and Mosegaard K., 2006, Linear inverse Gaussian
45
46 theory and geostatistics: Geophysics, **71**, R101-R111.

1
2
3
4
5
6
7
8
9
10
11
12
13
14
15
16
17
18
19
20
21
22
23
24
25
26
27
28
29
30
31
32
33
34
35
36
37
38
39
40
41
42
43
44
45
46
47
48
49
50
51
52
53
54
55
56
57
58
59
60

1
2
3
4
5
6
7
8
9
10
11
12
13
14
15
16
17
18
19
20
21
22
23
24
25
26
27
28
29
30
31
32
33
34
35
36
37
38
39
40
41
42
43
44
45
46
47
48
49
50
51
52
53
54
55
56
57
58
59
60

Harris, C., and M. Stephens., 1988, A Combined Corner and Edge Detector. *in* C. J. Taylor, eds, Proceedings of the Alvey Vision Conference: Alvey Vision Club, 23.1-23.6. doi:10.5244/C.2.23.

Hermans T., Kemna A., Nguyen F. 2016. Covariance-constrained difference inversion of time-lapse electrical resistivity tomography data. *Geophysics*, **81**, E311-E322.

Hermans T., Vandenbohede A., Lebbe L., Martin R., Kemna A., Beaujean J. and Nguyen F., 2012, Imaging artificial salt water infiltration using electrical resistivity tomography constrained by geostatistical data: *Journal of Hydrology*, 438-439, 168-180.

Idier, J., 2013. Bayesian Approach to Inverse Problems: John Wiley & Sons.

Kaipio J.P., Kolehmainen V., Vauhkonen M. and Somersalo E., 1999, Inverse problems with structural prior information: *Inverse problems*, 15, 713-729.

Johnson T.C., Versteeg, R.J., Rockhold M., Slater, L.D., Ntarlagiannis D., Greenwood W.J. and Zachara J., 2012, Characterization of a contaminated wellfield using 3D electrical resistivity tomography implemented with geostatistical, discontinuous boundary, and known conductivity constraints: *Geophysics*, **77**, EN85-EN96.

Johnson T.C., Routh P.S., Clemo T., Barrash W. and Clement W.P., 2007, Incorporating geostatistical constraints in nonlinear inversions problems: *Water Resources research*, **43**, W10422.

Kass, M., and A., Witkin, 1987. Analyzing oriented patterns: *Computer Vision, Graphics, and Image Processing*. **37**, 362–385. doi:10.1016/0734-189X(87)90043-0

Kim, H.J., Song, Y., and K.H., Lee, 1999, Inequality constraint in least-squares inversion of geophysical data: *Earth Planets Space*, **51**, 255–260.

1
2
3
4
5
6
7
8
9
10
11
12
13
14
15
16
17
18
19
20
21
22
23
24
25
26
27
28
29
30
31
32
33
34
35
36
37
38
39
40
41
42
43
44
45
46
47
48
49
50
51
52
53
54
55
56
57
58
59
60

Minasny, B., and A.B., McBratney, 2005, The Matérn function as a general model for soil variograms: *Geoderma, Pedometrics* 2003, **128**, 192–207.

doi:10.1016/j.geoderma.2005.04.003

Oldenburg, D.W., Li, Y., and R.G., Ellis, 1997, Inversion of geophysical data over a copper gold porphyry deposit: A case history for Mt. Milligan: *GEOPHYSICS*, **62**, 1419–1431. doi:10.1190/1.1444246

Paciorek, C.J., M.J., Schervish, 2006, Spatial modelling using a new class of nonstationary covariance functions: *Environmetrics*, **17**, 483–506. doi:10.1002/env.785

Paradis, D., Tremblay, L., Lefebvre, R., Gloaguen, E., Rivera, A., Parent, M., Ballard, J.-M., Michaud and Y., Brunet, P., 2014, Field characterization and data integration to define the hydraulic heterogeneity of a shallow granular aquifer at a sub-watershed scale: *Environmental Earth Sciences*, **72**, 1325–1348. doi:10.1007/s12665-014-3318-2

Pidlisecky, A., Haber, E., and R., Knight, 2007, RESINVM3D: A 3D resistivity inversion package: *GEOPHYSICS*, **72**, H1–H10. doi:10.1190/1.2402499

Ramirez, A.L., Daily, W.D., Binley, A.M., LaBrecque, D.J., and D., Roelant, 1996, Detection of leaks in underground storage tanks using electrical resistance methods: *European Journal of Environmental and Engineering Geophysics*, **1**, 189–203.

Sampson, P., 2010. Constructions for Nonstationary Spatial Processes, *in*: Gelfand, A., Diggle, P., Fuentes, M., and P., Guttorp, P., *Handbook of Spatial Statistics*: CRC Press, 119–130.

Saunders J.H., Herwanger J.V., Pain C.C. and Wothington M.H. 2005, Constrained resistivity inversion using seismic data: *Geophysical Journal International*, **160**, 785-796.

1
2
3
4 Shamsipour, P., Marcotte, D., Chouteau, M., Rivest, M., and A., Bouchedda, 2013, 3D
5 stochastic gravity inversion using nonstationary covariances: *GEOPHYSICS*, **78**, G15–
6 G24. doi:10.1190/geo2012-0122.1
7

8
9
10 Stein, M.L., 1999, *Interpolation of Spatial Data: Some Theory for Kriging*: Springer
11 Science & Business Media.
12

13
14
15 Tarantola, A., 2005, *Inverse problem theory and methods for model parameter*
16 *estimation*: Society for Industrial and Applied Mathematics, Philadelphia, PA.
17

18
19
20 Tarantola, A., and B., Valette, 1982, Generalized nonlinear inverse problems solved
21 using the least squares criterion: *Reviews in Geophysics*, **20**, 219.
22
23 doi:10.1029/RG020i002p00219
24
25

26
27 Tikhonov, A.N., and V.Y., Arsenin, 1977. *Solutions of ill-posed problems*: Winston.
28

29
30 Tremblay, L., Lefebvre, R., Paradis, D., and E., Gloaguen, 2013, Conceptual model of
31 leachate migration in a granular aquifer derived from the integration of multi-source
32 characterization data (St-Lambert, Canada): *Hydrogeological Journal*, **22**, 587–608.
33
34
35 doi:10.1007/s10040-013-1065-1.
36
37

38
39
40 Ulrych, T.J., Sacchi, M.D. and Woodbury, A., 2001, A Bayes tour of inversion: A
41 tutorial: *GEOPHYSICS*, **66**, 55-69.
42

43
44
45 Whittle, P., 1963. *Stochastic processes in several dimensions*: *Bulletin of the*
46 *International Statistical Institute*, **40**, 974–994.
47

48
49
50 Whittle, P., 1954, On stationary processes in the Plane: *Biometrika*, **41**, 434–449.
51
52 doi:10.1093/biomet/41.3-4.434.
53

54
55
56 Yang X. and LaBrecque D.J., 1998, Stochastic inversion of 3D ERT data: *Symposium on*
57 *the Application of Geophysics to Engineering and Environmental Problems*, *EEGS*, **11**,
58 221-228.
59
60

Yeh T.-C. and Liu S. 2000. Hydraulic tomography: Development of a new aquifer test method: Water Resources Research, **36**, 2095-2105.

Zhou J., A. Revil, M. Karaoulis, D. Hale, J. Doetsch, and S. Cuttler, 2014, Image-guided inversion of electrical resistivity data: Geophysical Journal International, **197**, 292-309, doi:10.1093/gji/ggu001

1
2
3
4
5
6
7
8
9
10
11
12
13
14
15
16
17
18
19
20
21
22
23
24
25
26
27
28
29
30
31
32
33
34
35
36
37
38
39
40
41
42
43
44
45
46
47
48
49
50
51
52
53
54
55
56
57
58
59
60

FIGURE CAPTIONS

Figure 1: Smooth inversion results of Model 1 data. (a) true resistivity model, smooth inversion model (b) without constraints, (c) with constraints at the 1 m deep interface, (d) with constraints at the 1 m and 2 m deep interfaces, (e) with $\alpha_z=0.2$ and (f) with constraints at the 1 m and 2 m deep interfaces and $\alpha_z=0.2$. The white lines represent the true interfaces.

Figure 2: Experimental isotropic semi-variogram obtained using smooth inversion resistivity image.

Figure 3: Effect of variations of the range parameter r on Bayesian inversion results. (a) $r=2$ m, (b) $r=4$ m, (c) $r=6$ m, (d) $r=8$ m, (e) $r=10$ m and (f) $r=20$ m. The white lines represent the true interfaces.

Figure 4: Effect of variations of the standard deviation (STD) on Bayesian inversion results. (a) $\delta=10$ $\Omega.m$, (b) $\delta=50$ $\Omega.m$, (c) $\delta=100$ $\Omega.m$, (d) $\delta=1000$ $\Omega.m$. The white lines represent the true interfaces.

Figure 5: Bayesian inversion results of model 1 data using $r = 8$ m, $\delta=100$ $\Omega.m$, $g=(1, 0)$ and in (a) model 1, (b) $v=1$, (c) $v=2$, (d) $v=2.5$, (e) $v=3$, (f) $v=4$. The white lines represent the true interfaces.

Figure 6: Inversion results using non-stationary correlation (a) model 1, (b) smooth inversion model with anisotropic smoothness factor, (c) (a) with additional constraints on interfaces at 1 m and 2 m depths; Bayesian inversion model resulting from using spatially varying range with (d) $v=1$, (e) $v=1.5$ and (f) $v=3$. The white lines represent the true interfaces.

1
2
3
4
5
6
7
8
9
10
11
12
13
14
15
16
17
18
19
20
21
22
23
24
25
26
27
28
29
30
31
32
33
34
35
36
37
38
39
40
41
42
43
44
45
46
47
48
49
50
51
52
53
54
55
56
57
58
59
60

Figure 7: Inversion results of Model 2; (a) synthetic model, (b) smooth inversion, Bayesian inversion model with (c) $\nu=1$, (d) $\nu=2.5$, (e) $\nu=3$ and (f) $\nu=4$. The true interfaces are indicated with white lines; surface and borehole electrodes are represented by black circles and triangles respectively.

Figure 8: Inversion results using structural anisotropy; (a) synthetic model, Bayesian inversion model with (b) $\nu=1$, (c) $\nu=1$ and $m_{\text{prior}}=\log(1000)$, (d) $\nu=1$ and $m_{\text{prior}}=\log(10000)$, (e) $\nu=1$ and $g=(-1/2, 1/2)^T$ on all grid points and (f) $\nu=1$ and $g=(0, 1)^T$ in the centre of panel (vertical dyke). The true interfaces are indicated with white lines; surface and borehole electrodes are represented by black circles and triangles respectively.

Figure 9: Study area location. (a-b) general location, (c) study area limits with surface geological information, geophysical surveys, CPT and observation well location (modified from Paradis et al. (2014)). The GPR and ERT line presented in this work is indicated by red arrow.

Figure 10: GPR section and inversion results of Saint-Lambert data; (a) smooth inversion model, (b) smooth inversion model with anisotropic smoothing factor ($l_z/l_x=5$) and (c) GPR section. GPR interfaces are shown as white lines on resistivity images and as red lines on GPR section.

Figure 11: GPR section (a) and inversion results of Saint-Lambert data using structural anisotropy; Bayesian inversion model with (a) $\nu=1$, (b) $\nu=1.5$. GPR interfaces are shown as white lines and red arrows represent structure orientations.

TABLE CAPTIONS

Table 1 : The equivalent of the Matérn covariance function (Minasny and McBratney, 2005).

1
2
3
4
5
6
7
8
9
10
11
12
13
14
15
16
17
18
19
20
21
22
23
24
25
26
27
28
29
30
31
32
33
34
35
36
37
38
39
40
41
42
43
44
45
46
47
48
49
50
51
52
53
54
55
56
57
58
59
60

TABLES

	Equivalent function	Approximate function
	$r > 0$, Bounded	$r \rightarrow \infty$, Unbounded
$\nu \rightarrow 0$		De Wijs: $-\log(h)$
$\nu > 0$, integer		$-h^{2\nu} \log(h)$
$\nu > 0$, non-integer		Power: $-h^{2\nu}$
$\nu = 0.5$	Exponential: $\exp(-h / r)$	
$\nu = 1$	Whittle: $(h / r) K_1(h / r)$	$-h^2 \log(h)$
$\nu \rightarrow \infty$	Gaussian: $\exp(-h^2 / r^2)$	

Table 1 : The equivalent of the Matérn covariance function (Minasny and McBratney, 2005).

1
2
3
4
5
6
7
8
9
10
11
12
13
14
15
16
17
18
19
20
21
22
23
24
25
26
27
28
29
30
31
32
33
34
35
36
37
38
39
40
41
42
43
44
45
46
47
48
49
50
51
52
53
54
55
56
57
58
59
60

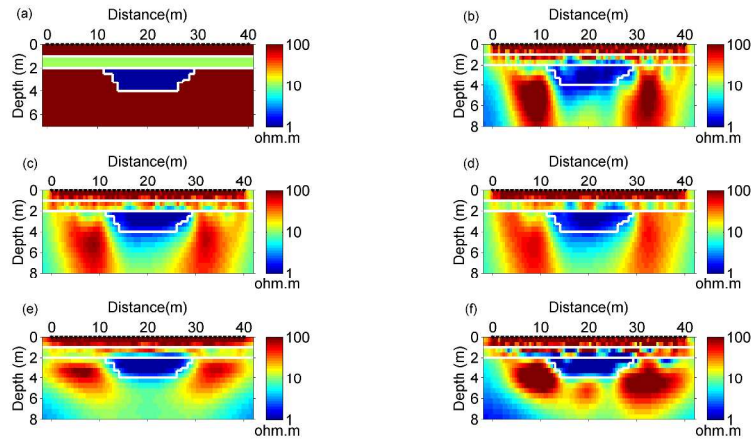


Figure 1: Smooth inversion results of Model 1 data. (a) true resistivity model, smooth inversion model (b) without constraints, (c) with constraints at the 1 m deep interface, (d) with constraints at the 1 m and 2 m deep interfaces, (e) with $\alpha=0.2$ and (f) with constraints at the 1 m and 2 m deep interfaces and $\alpha=0.2$. The white lines represent the true interfaces.

Figure 1
423x207mm (300 x 300 DPI)

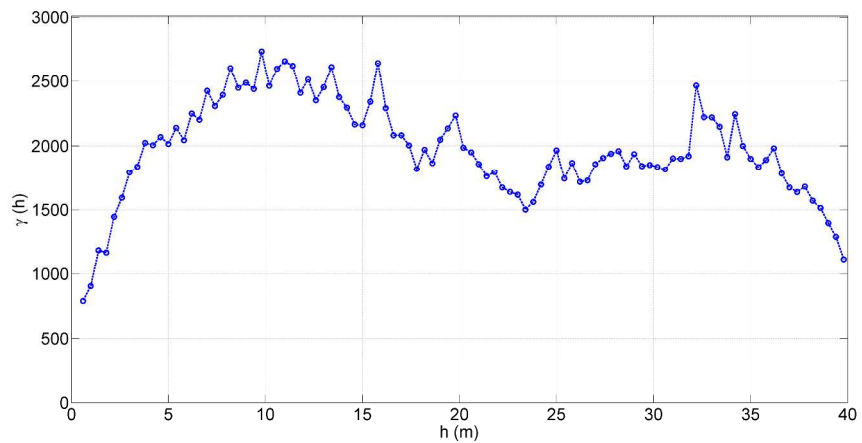


Figure 2: Experimental isotropic semi-variogram obtained using smooth inversion resistivity image.

Figure 2
423x200mm (300 x 300 DPI)

1
2
3
4
5
6
7
8
9
10
11
12
13
14
15
16
17
18
19
20
21
22
23
24
25
26
27
28
29
30
31
32
33
34
35
36
37
38
39
40
41
42
43
44
45
46
47
48
49
50
51
52
53
54
55
56
57
58
59
60

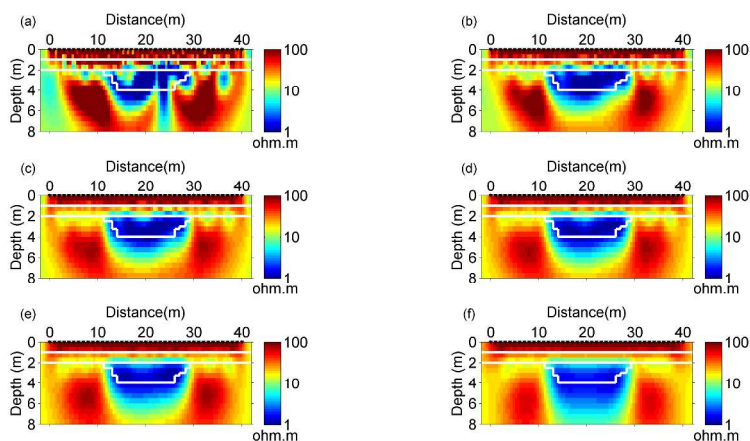


Figure 3: Effect of variations of the range parameter r on stochastic inversion results. (a) $r=2$ m, (b) $r=4$ m, (c) $r=6$ m, (d) $r=8$ m, (e) $r=10$ m and (f) $r=20$ m. The white lines represent the true interfaces.

Figure 3
423x207mm (300 x 300 DPI)

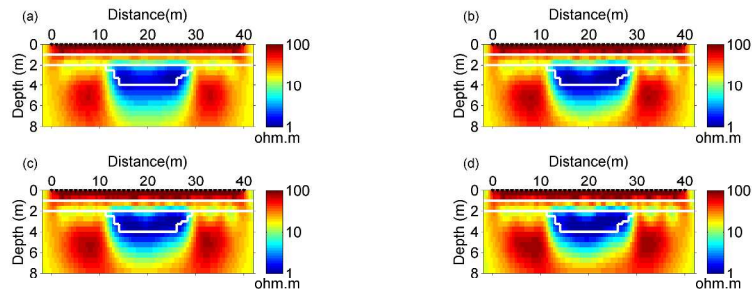


Figure 4: Effect of variations of the standard deviation (STD) on stochastic inversion results. (a) $\delta = 10$ ohm.m, (b) $\delta = 50$ ohm.m, (c) $\delta = 100$ ohm.m, (d) $\delta = 1000$ ohm.m. The white lines represent the true interfaces.

Figure 4
423x207mm (300 x 300 DPI)

1
2
3
4
5
6
7
8
9
10
11
12
13
14
15
16
17
18
19
20
21
22
23
24
25
26
27
28
29
30
31
32
33
34
35
36
37
38
39
40
41
42
43
44
45
46
47
48
49
50
51
52
53
54
55
56
57
58
59
60

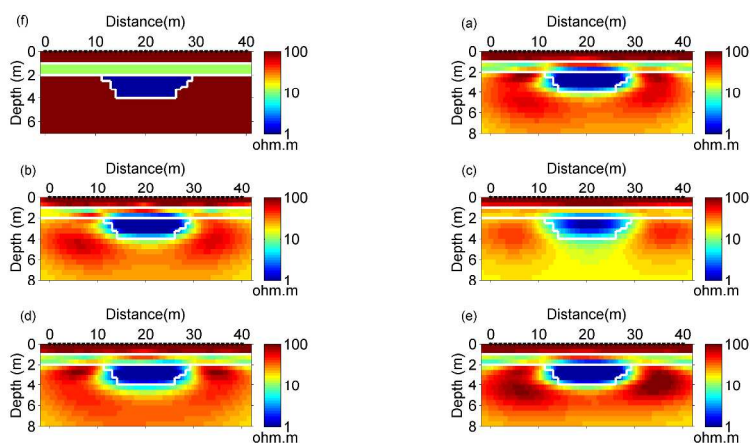


Figure 5: Stochastic inversion results of model 1 data using $r = 8 \text{ m}$, $\delta = 100 \Omega \cdot \text{m}$, $g = (1, 0)$ and in (a) model 1, (b) $\nu = 1$, (c) $\nu = 2$, (d) $\nu = 2.5$, (e) $\nu = 3$, (f) $\nu = 4$. The white lines represent the true interfaces.

Figure 5
423x207mm (300 x 300 DPI)

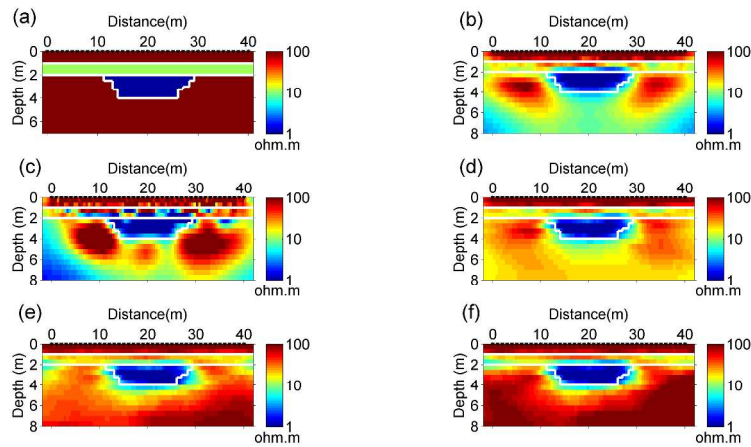


Figure 6: Inversion results using non-stationary correlation (a) model 1, (b) smooth inversion model with anisotropic smoothness factor, (c) (a) with additional constraints on interfaces at 1 m and 2 m depths; stochastic inversion model resulting from using spatially varying range with (d) $\nu=1$, (e) $\nu=1.5$ and (f) $\nu=3$. The white lines represent the true interfaces.

Figure 6
423x207mm (300 x 300 DPI)

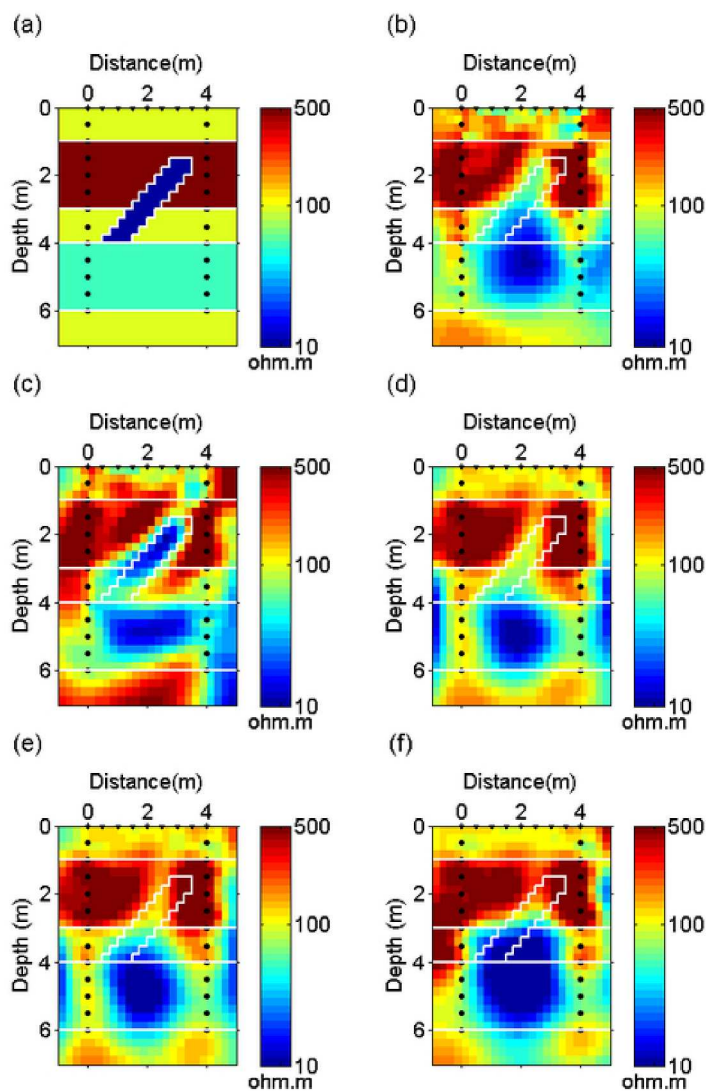


Figure 7: Inversion results of Model 2; (a) synthetic model, (b) smooth inversion, stochastic inversion model with (c) $\nu=1$, (d) $\nu=2.5$, (e) $\nu=3$ and (f) $\nu=4$. The true interfaces are indicated with white lines; surface and borehole electrodes are represented by black circles and triangles respectively.

Figure 7
199x282mm (300 x 300 DPI)

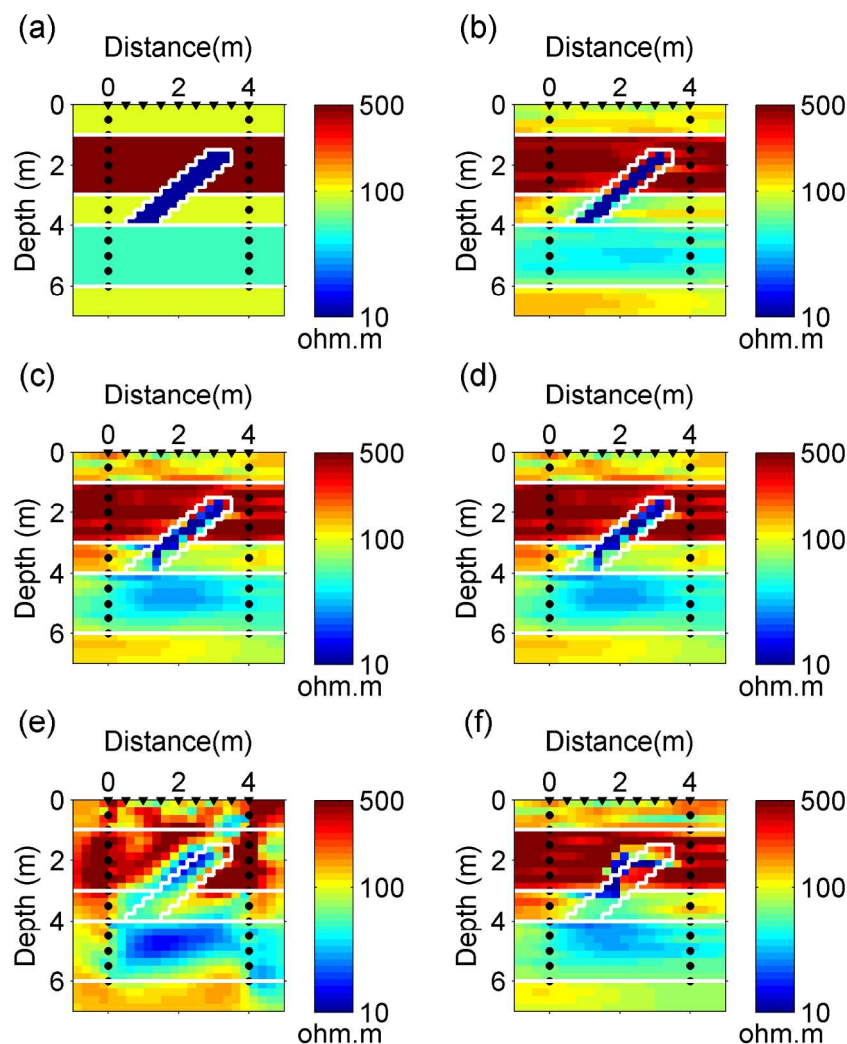


Figure 8: Inversion results using structural anisotropy; (a) synthetic model, stochastic inversion model with (b) $\nu=1$, (c) $\nu=1$ and $m_{\text{prior}}=\log(1000)$, (d) $\nu=1$ and $m_{\text{prior}}=\log(10000)$, (e) $\nu=1$ and $g=(-1/2, 1/2)^T$ on all grid points and (f) $\nu=1$ and $g=(0, 1)^T$ in the centre of panel (vertical dyke). The true interfaces are indicated with white lines; surface and borehole electrodes are represented by black circles and triangles respectively.

Figure 8
176x204mm (300 x 300 DPI)

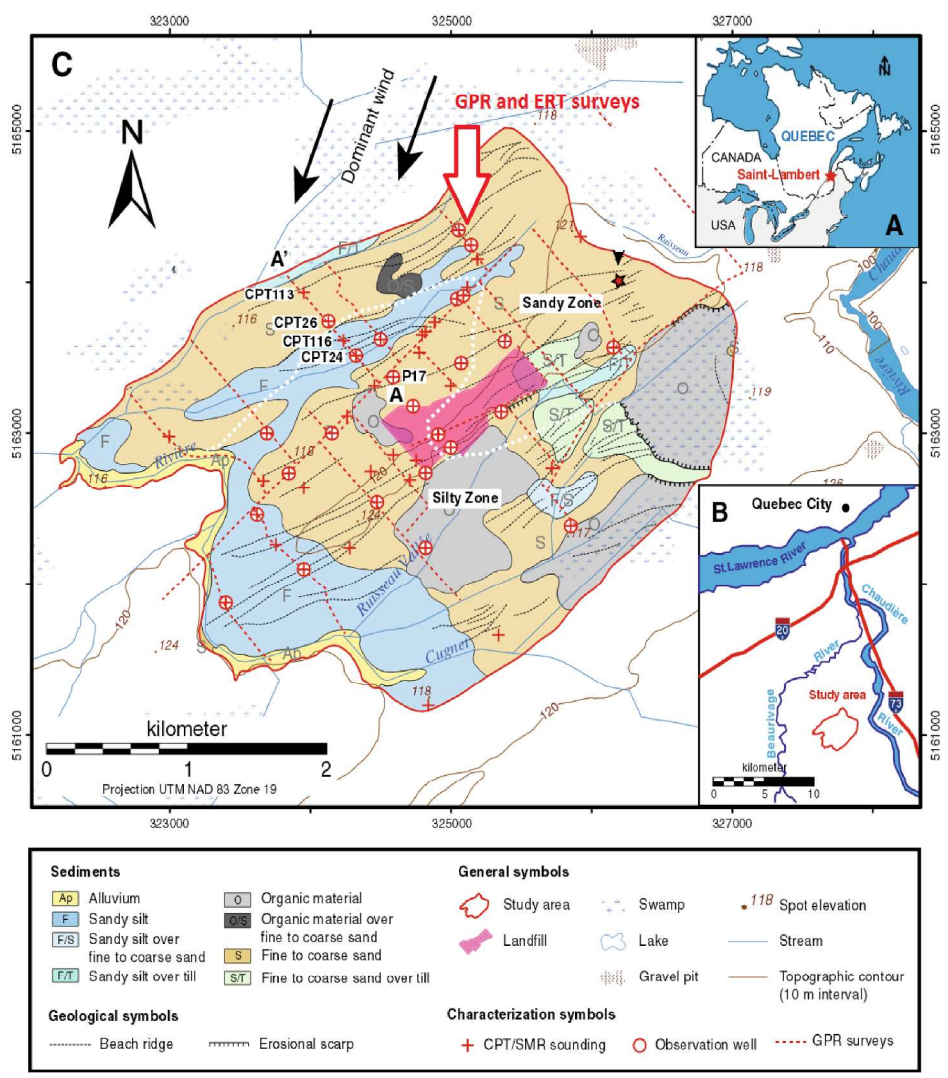


Figure 9: Study area location. (a-b) general location, (c) study area limits with surface geological information, geophysical surveys, CPT and observation well location (modified from Paradis et al. (2014). The GPR and ERT line presented in this work is indicated by red arrow.

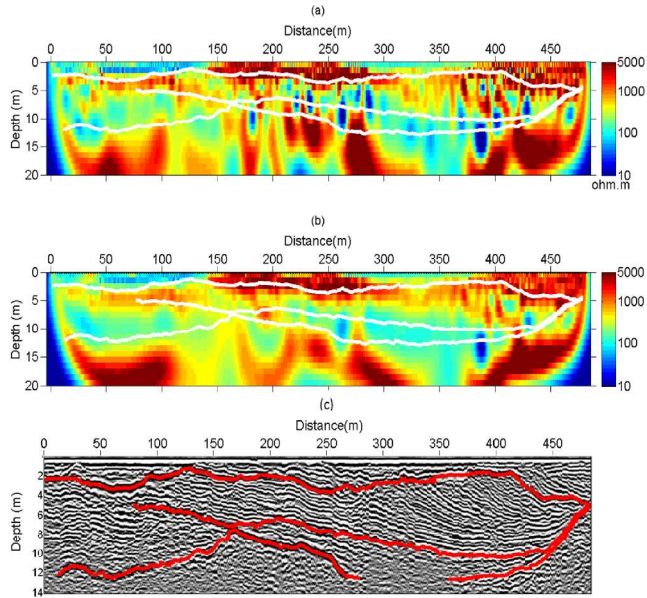


Figure 10: GPR section and inversion results of Saint-Lambert data; (a) smooth inversion model, (b) smooth inversion model with anisotropic smoothing factor ($l_z/l_x=5$) and (c) GPR section. GPR interfaces are shown as white lines on resistivity images and as red lines on GPR section.

Figure 10

318x265mm (300 x 300 DPI)

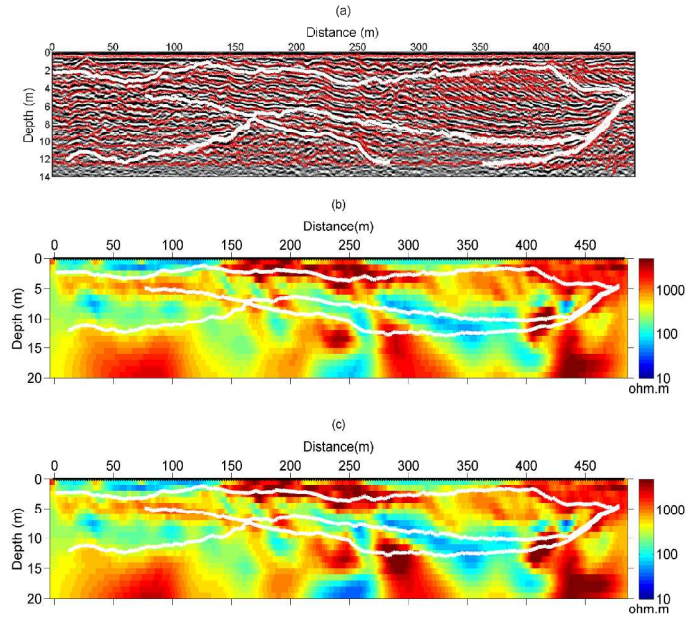


Figure 11: GPR section (a) and inversion results of Saint-Lambert data using structural anisotropy; Stochastic inversion model with (a) $v=1$, (b) $v=1.5$. GPR interfaces are shown as white lines on ERT images and red arrows in GPR section represent structure orientations.

Figure 11
307x233mm (300 x 300 DPI)